J. Indian Inst. Sci., Mar.–Apr., 2002, **82**, 93–103

Brillouin scattering studies on charge-ordered manganites*

CHANDRABHAS NARAYANA
Chemistry and Physics of Materials Unit, Jawaharlal Nehru Centre for Advanced Scientific Research, Bangalore 560 064, India.
email: cbhas@jncasr.ac.in, Ph: +91-80-846 2750 Ext. 2244; Fax: +91-80-846 2766.

Abstract

Brillouin scattering studies were carried out for the first time on charge-ordered manganites, namely, $Nd_{0.5}Ca_{0.5}MnO_3$ and $Pr_{0.63}Ca_{0.37}MnO_3$. We observe surface and bulk magnetic excitations (magnons) in the Brillouin spectra with the characteristics of ferromagnetic magnons. The frequency and intensity of these magnons in the temperature range 300 to 25 K, covering both charge-ordering and antiferromagnetic transition, follow exactly the temperature dependence of the DC magnetic susceptibility. The study strongly suggests the presence of ferromagnetic inhomogeneities in the charge-ordered as well as antiferromagnetic phases.

Keywords: Brillouin scattering, charge-ordering, magnon and manganites.

1. Introduction

The ground state of doped manganites, with the general formula $R_{1-x}A_xMnO_3$ (R = rare earth, e. g. La, Pr, A = alkaline earth metal, e. g. Ca, Sr) can be a ferromagnetic (FM) and metallic or a charge-ordered insulator state, depending on the extent of doping, *x*, and the tolerance factor [1], [2]. When the weighted average of A site cation radius is small, the Mn-O-Mn bond angle deviates from 180°, reducing the transfer integral and hence the e_g electron bandwidth of Mn^{3+} ions. This causes real space ordering (charge-ordering) of the Mn^{3+} and Mn^{4+} ions. Ferromagnetism in the manganites is qualitatively understood in terms of Zener's double exchange, which connects electron hopping with the FM alignment of the Mn t_{2g} electron spins [3], [4]. In recent years, charge localization has been invoked along with double exchange due to the lattice polarons formed by Jahn–Teller (JT) distortion around the Mn^{3+} ion [5]. The formation of magnetic polarons to localize the charge carriers has also been proposed [6].

Recent electron and neutron diffraction experiments have shown the coexistence of an incommensurate charge-ordered phase within the FM metallic phase in $La_{0.5}Ca_{0.5}MnO_3$ [7]. The incommensurate state is considered to involve partial orbital ordering in spite of complete charge-ordering. A transmission electron microscopy (TEM) study of insulating $Pr_{0.5}Ca_{0.5}MnO_3$ has shown the occurrence of the incommensurate to commensurate charge-ordering transition coincident with the antiferromagnetic (AFM) spin ordering transition at 180 K [8].

Brillouin scattering studies of charge-ordered manganites has been carried out to examine the role of magnetic excitations across the charge-ordering and AFM transitions to elucidate the role of couplings between the lattice, the charge carriers and the magnetic excitations. For this purpose, we have chosen $Nd_{0.5}Ca_{0.5}MnO_3$ (NCMO) and $Pr_{0.63}Ca_{0.37}MnO_3$ (PCMO), which re-

* Text of lecture delivered at the Annual Faculty Meeting of the Jawaharlal Nehru Centre for Advanced Scientific Research at Bangalore on November 17, 2001.

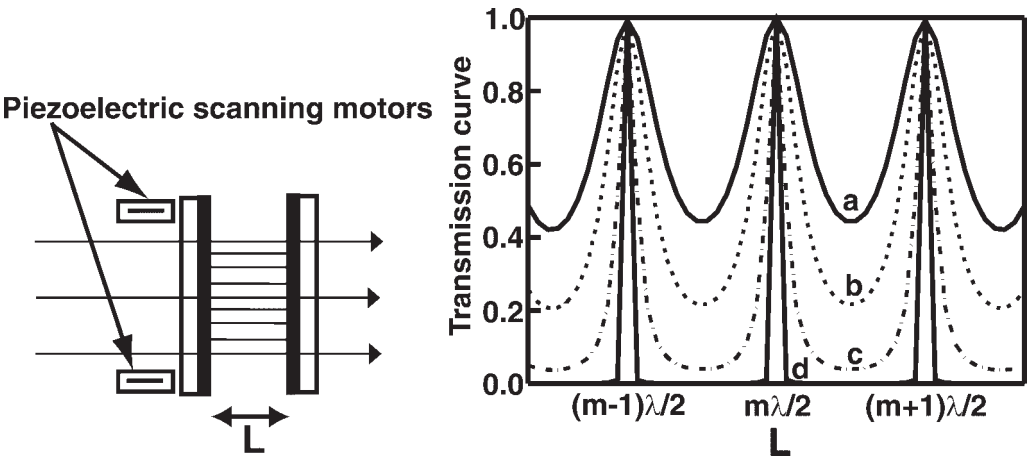

Fig. 1. A schematic representation of the Fabry–Perot interferometer and its transmission spectrum. Curves a to d represent the number of passes through the FP, where curves a and d represent single and six passes, respectively.

mains an insulator at all temperatures and shows a transition from a paramagnetic (PM) insulating state to a charge-ordered (CO) state ($T_{CO} \sim 250$ K) and from the CO state to an AFM state ($T_N \sim 150$ K) [9].

2. Brillouin light scattering spectrometer

In a typical Brillouin scattering experiment we observe both acoustic and spin waves with frequencies in the range between about 1 and 150 GHz. In order to extract the weak inelastic component of light from the elastically scattered contribution, a high-resolution spectrometer is required. This is achieved by using a Fabry–Perot (FP) interferometer as a scanning spectrometer with best combination of high resolution and good throughput. FP interferometer consists of two very flat mirrors mounted accurately parallel to each other with a variable spacing. For a fixed distance, L, the interference condition is such that only the light of wavelength λ will be transmitted, with $L = m\,\lambda/2$ where m is an integer. Therefore, this instrument acts as a bandpass frequency filter whose peak transmission is close to unity over a narrow spectral interval (Fig. 1).

The interference orders are separated in frequencies by $c/2L$ Hz, where c is the speed of light. This interorder spacing is called the free spectral range (FSR). The width of the transmission peak determines the resolution of the instrument. The ratio of FSR to width is known as the finesse F. The value of F depends on the mirror reflectivity, R, instrumental aperture and mirror flatness. But in practice, the finesse is limited to values less than about 100 and this places an upper limit on the possible contrast C, which is the ratio of maximum to minimum transmission given by $C = 1 + 4F^2/\pi^2$.

In opaque materials, it is usual that the elastically scattered light exceeds the intensity of the Brillouin component by more than a factor of 10^4–10^5. Thus, the above contrast is not sufficient for measuring in such a situation. A way for increasing the spectral contrast is the introduction of the multipass operation. Sending back and forth a few times the light through the same interferometer does this. By this way, the contrast can be increased up to values close to 10^{10} and this would be sufficient for Brillouin scattering experiments in opaque materials.

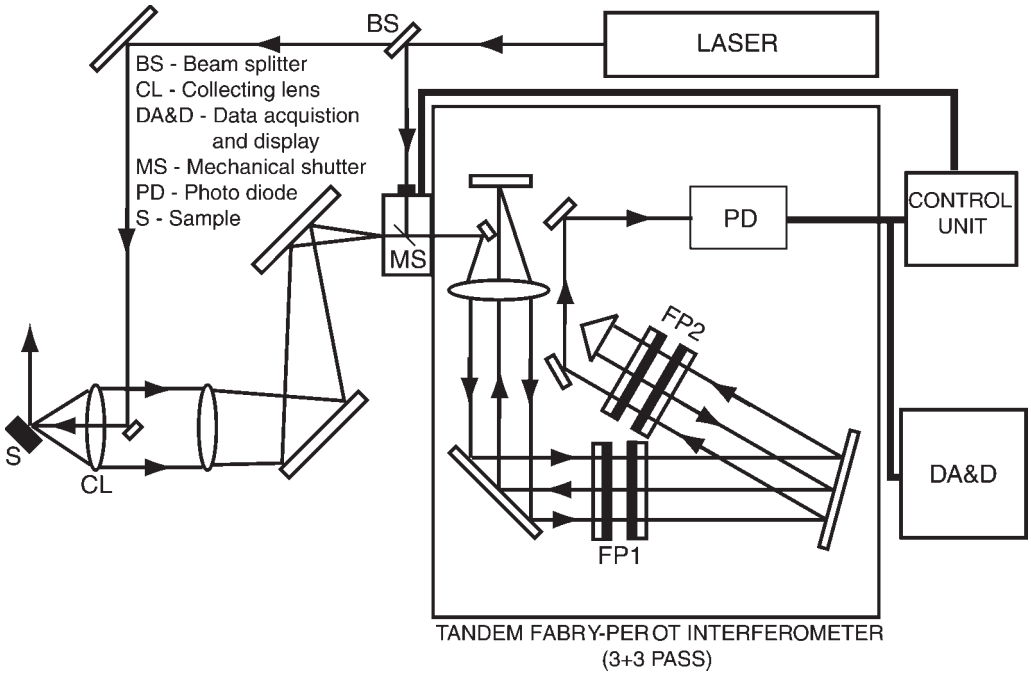

Fig. 2. A schematic representation of the whole experimental set-up in the backscattering geometry used in the present paper. The rays represent the laser beam path. The set-up shows the 3 + 3 pass (multipass) tandem Fabry–Perot interferometer (labeled FP1 and FP2).

In order to avoid the overlap of neighboring interference order and extend the range of frequency investigated (or the FSR), it is possible to combine two interferometers of unequal mirror spacing (tandem operation), as shown in Figs 2 and 3a. The first interferometer of spacing L_1 transmits wavelengths $L_1 = 2\lambda/m_1$ for integral m_1, while the second interferometer of spacing L_2 transmits wavelengths $L_2 = 2\lambda/m_2$ for integral m_2. Only if $L_1 = L_2$ light will be transmitted through the combination. It is important to notice, however, that to scan the transmitted wavelength, it is necessary to increment the mirror spacing L_1 and L_2 by ΔL_1 and ΔL_2 such that $\Delta L_1/ L_1 = \Delta L_2/ L_2$.

In the Sandercock interferometer (spectrometer used for this work) this condition is achieved mounting the interferometers on the same scanning stage, one with the mirror axis parallel to the scan direction, the other offset by an angle θ. It is clear that the spacing of the two interferometers satisfies the equation $L_2 = L_1 \cos\theta$ as shown in Fig. 3a. The synchronization condition given above is thus satisfied. In this way, it is possible to increase the FSR by a factor 10–20 over that of the single interferometer, although as shown in Fig. 3b, small ghosts remain of the suppressed orders.

Given the low intensity of the Brillouin signals, single-photon counting is necessary for the detection system. Quite recently a new generation of low-background noise, single-photon avalanche photodiodes with quantum efficiency higher than a typical photomultiplier tube is available and is used in the present experimental system to detect the signal.

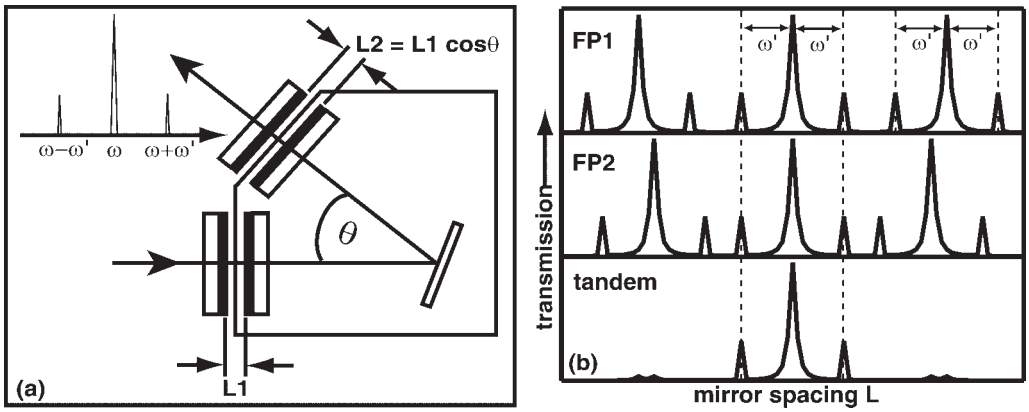

Fig. 3a. A schematic representation of the tandem Fabry–Perot interferometer, b. shows the transmission spectrum through individual Fabry–Perot and in combination (tandem).

3. Experimental details

Polycrystalline NCMO was prepared by the solid-state reaction of Nd_2O_3, $CaCO_3$ and MnO_2 at 1273 K for 24 h, followed by sintering at 1373 K for 24 h in flowing oxygen. Powder X-ray diffraction at room temperature showed the material to be orthorhombic with a Mn^{4+} content ~ 52% as determined by redox titration [9]. The single crystals of NCMO were grown using floating zone furnace (NEC, Japan). The T_{CO} and T_N were measured from the magnetization measurements using the vibrating sample magnetometer (VSM) (Model No. 7300, LakeShore, USA).

Single crystalline rod of PCMO, which was cut along (100) plane in the growth direction, was obtained from the Joint Research Center for Atom Technology (JRCAT), Tsukuba, Japan, for our present study.

Brillouin scattering measurements were carried out on a disk of 6-mm diameter and ~ 3 mm thick cut from the single crystalline rod of NCMO and PCMO. Spectra were excited using single-mode 532 nm radiation from diode-pumped frequency-doubled Nd-YAG laser (Coherent Model DPSS No. 532-400) in the backscattering geometry with angle of incidence of $\alpha = 45^o$ and polarization in the plane of the incidence (Fig. 2). Spectra were recorded using (3+3) pass tandem Fabry–Perot interferometer (JRS Scientific Instruments, Switzerland) with a finesse of ~100 and free spectral range of 85 GHz [10]. The temperature-dependent measurements were carried out from 300 to 27 K with the crystal inside a closed cycle helium cryostat, with the temperature stability of ± 0.01 K. Measurements were also carried out at room temperature in the presence of magnetic field (up to 0.3 T using an electromagnet), nearly perpendicular to the plane of the sample (Fig. 4 inset).

4. Results and discussion

Figure 4a shows a typical Brillouin spectrum of NCMO at room temperature in the absence of a magnetic field. Here open circles show the data and the solid lines are fits to Lorentzian with appropriate background. The inset shows the scattering geometry. Two modes at frequencies ν_B

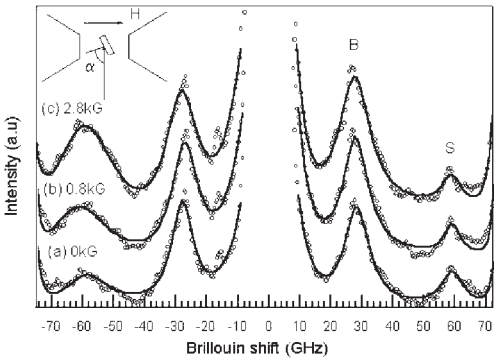

Fig. 4. Brillouin spectra at different external magnetic field, (a) H = 0, (b) 0.08 T, and (c) 0.28 T. Inset shows the scattering geometry where the magnetic field H (nearly perpendicular to the plane of the sample) is generated by the electromagnet. α is the angle of incidence with respect to the normal. Open circles are data points and solid lines are fits to Lorentzian functions with appropriate background.

~ 27 GHz (labeled B mode) and ν_S ~ 60 GHz (labeled S mode) are easily identified in the spectra. The S-mode is weak at room temperature and remains so even at lower temperatures.

We have therefore followed only the B-mode as a function of temperature. Figure 5a shows the temperature-dependence of the B-mode frequency (ν_B) and Fig. 6, the temperature-dependence of its intensity (A) and full width at half maximum (Γ) from 300 to 27 K in the cooling run.

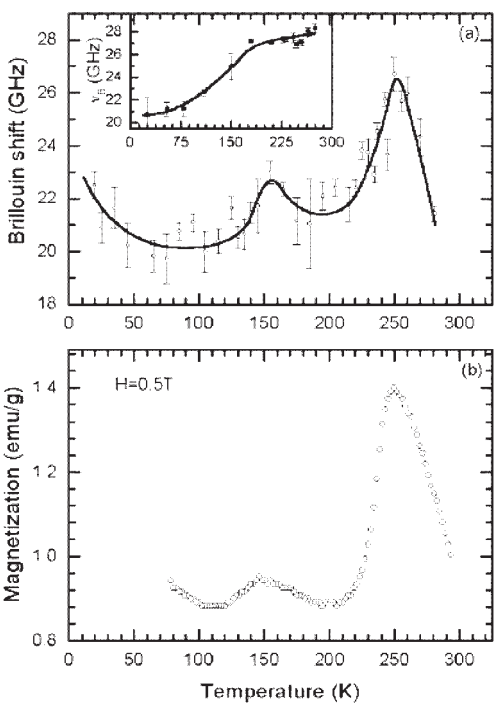

Fig. 5a. Temperature–dependence of the B-mode in the cooling cycle. The inset (a) shows the heating cycle. b. Temperature-dependence of magnetization measured using VSM in a field of 0.5 T. The solid lines are drawn as a guide to the eye.

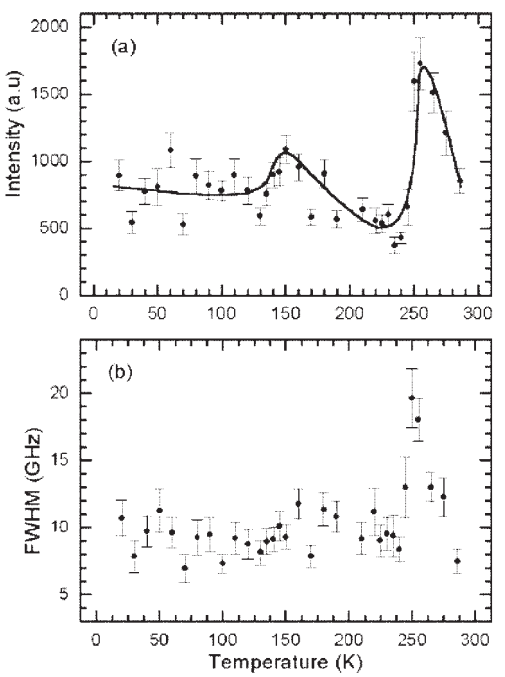

Fig. 6. Temperature-dependence of a. intensity and b. linewidth of the B-mode. The solid line is drawn as guide to the eye.

Interestingly, ν_B and A closely follow the temperature-dependence of the d.c. magnetic susceptiblity of the same sample shown in Fig. 5b. The observation that ν_B and A are both proportional to the d.c. magnetic susceptibility (χ) strongly suggests that the B-mode is associated with the magnetic excitations of the medium. To check this further, experiments were carried out at room temperature as a function of total wave vector transfer q and its component parallel to the surface, $q_\parallel$. The dependence on q is not entirely conclusive due to the limited range of available q (4 to 4.5 x 10^5 cm^{-1}). However, the S-mode frequency varies as a function of $q_\parallel$ as shown in Fig. 7a. These experiments were done in the backscattering geometry with varying angle α, which keeps q constant. It is seen that the B-mode does not depend on $q_\parallel$, whereas the S-mode frequency increases linearly with $q_\parallel^2$, suggesting thereby that the S-mode is associated with surface magnon excitations and the B-mode with bulk magnons. This is further corroborated by the hysteresis observed in the temperature-dependence of ν_B as shown in the inset of Fig. 5a, because such hysteresis is not normally expected to occur for acoustic phonons.

It is to be noted here that similar hysteresis has not been observed in the studies carried out on PCMO. In fact, the temperature-dependent magnetization behavior of NCMO also shows the

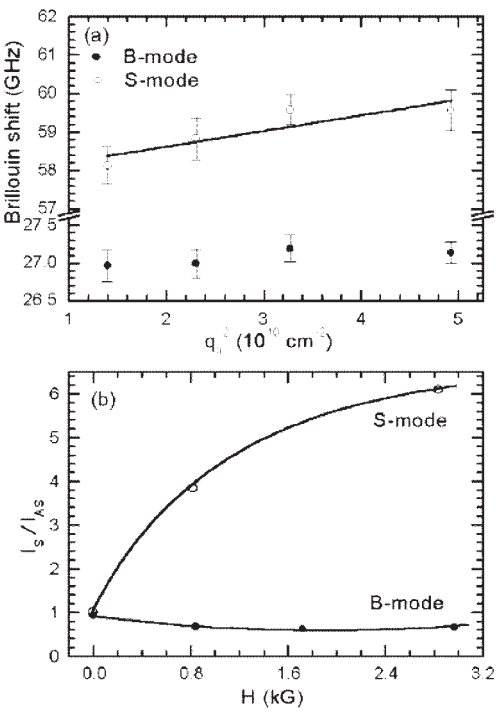

Fig. 7a. Mode frequencies as a function of $q_\parallel^2$. The solid line is a fit to the linear equation. b. Ratio of Stokes and antiStokes intensities as a function of applied magnetic field at room temperature. The solid lines are guide to the eye.

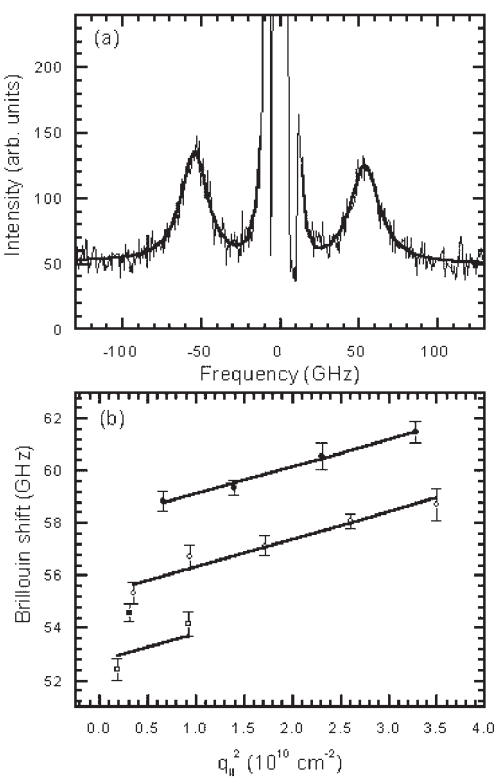

Fig. 8a. Room-temperature Brillouin spectrum of $Pr_{0.67}Ca_{0.37}MnO_3$. b. Mode frequency as a function of $q_\parallel^2$ performed in different geometry (from top 180°, 90° and 30°). The solid lines are fits to a. lorentzian and b. linear equation.

hysteresis, namely, in the heating cycle the antiferromagetic ordering appears as a weak shoulder. This has also been observed in PCMO (half-doped) by Mahendiran *et al.* [11] in both temperature-dependent magnetization studies as well as modulation vector studied using electron microscopy. The origin of this hysteresis is not yet understood. We believe that the hysteresis is due to the increase in ferromagnetic correlation at very low temperatures. It is also reported in the literature that in the case of half-doped manganites, at extremely low temperatures there is canting of spins in the CE-type antiferromagetic ordering. Upon heating they relax slowly to the charge and orbital ordered state.

In the case of PCMO, as shown in Fig. 8a, the room temperature spectrum shows only one mode, which is similar in frequency to the S-mode in the case of NCMO. The mode has similar behavior to the S-mode, that is, it has a linear dependence on $q_{\|}^{2}$ and occurs at 59 GHz, similar to the NCMO. This is shown in Fig. 8b performed in different scattering geometry. Figure 9 shows the temperature-dependence of the frequency and the data of the d.c. magnetization has been superimposed over the Brillouin data (solid line in Fig. 9) with appropriate scaling to suggest, that frequency behavior is similar to d.c. magnetization. Inset in Fig. 9 shows the actual data of the d.c. magnetization, to give an idea of the scaling done. Figure 10 shows the temperature dependence of the intensity and FWHM of the 59 GHz mode. The behavior of the 59 GHz mode of PCMO along with its intensity and FWHM suggests that it is also a magnetic excitation associated with the medium and so is the S-mode of the NCMO.

It is known that the intensity and peak position of Brillouin lines originating from magnons depend on the external applied magnetic field. Experiment was, therefore, carried out at room temperature with the sample in a magnetic field up to 0.28 T. Curves b and c in Fig. 4 correspond to the spectra at 0.08 and 0.28 T, respectively. The peak positions do not change (to be discussed later), whereas the ratio of the Stokes to antiStokes intensities changes significantly for the S-mode, as shown in Fig. 7b. This change can occur because of the nonreciprocal propagation of the Damon–Eshback (DE) surface magnon mode [10], [12]. The DE mode can propagate only in a certain range of directions and therefore, the surface magnon is seen in either Stokes or anti-Stokes side of the spectrum in ferromagnets [13]. We believe that NCMO and PCMO is likely to possess magnetic domains expected in an orthorhombic system. This does not permit complete disappearance of the surface mode on one side of the spectrum at H = 0. However, application of a magnetic field aligns the domains and hence the asymmetry between Stokes and antiStokes intensities increases for the surface mode.

The higher surface magnon frequency relative to that of the bulk magnon implies that these are spin-wave excitations of a ferromagnet, for which frequencies are given by ($\omega_B = 2\pi\nu_B$) [14]:

$$\omega_B^{\,2} = \gamma^2(H + Dq^2)(H + Dq^2 + 4\pi M_S \sin^2\theta) \tag{1}$$

where γ is the gyromagnetic ratio, H, the external applied magnetic field, D, the exchange constant, M_S, the saturation magnetization and θ, the angle between q and M_S. The temperature-dependence of ω_B is determined by M_S, as indeed seen in Fig. 5a. The Damon–Eshbach surface spin wave has frequency ($\omega_S = 2\pi\nu_S$) [10], [12]:

$$\omega_S = \gamma/2[H/\sin\theta' + (H + 4\pi M_S)\sin\theta'] + \gamma D' q_{\|}^{\,2} \tag{2}$$

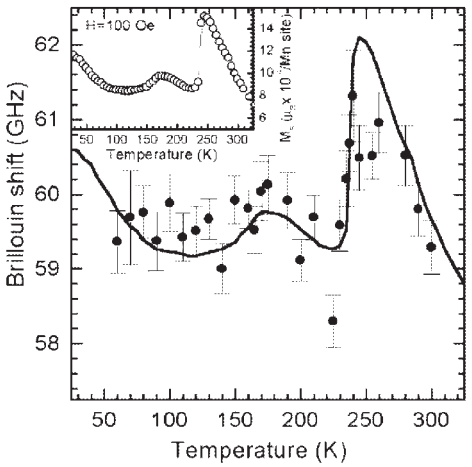

Fig. 9. Temperature-dependence of the surface magnon mode. The solid dots are the data points and the solid line is the d.c. magnetization data. The inset shows temperature-dependence of magnetization in a field of 100 Oe.

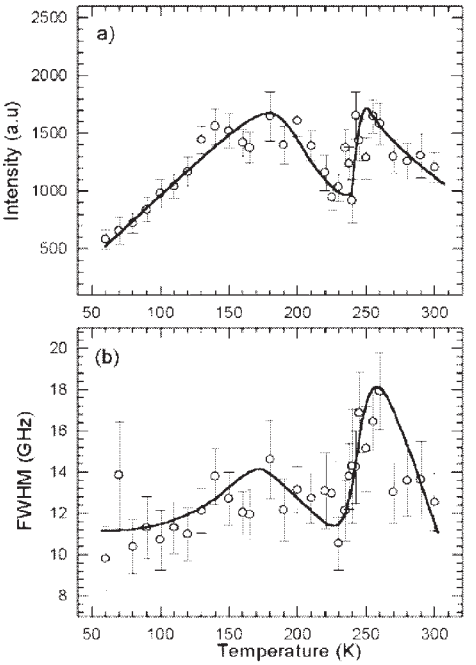

Fig. 10. Temperature-dependence of a. intensity, b. FWHM of the surface mode. The solid lines are guide to the eye.

where D′ ~2D and θ' is the angle between $q_{\|}$ and M_S [13]. It can be seen that $\omega_S > \omega_B$ for magnons in a ferromagnet. This is, however, not the case for magnons in antiferromagnets [14].

For H = 0, $$2\pi\nu_S = 2\pi\gamma M_S \sin\theta' + \gamma D' q_{\|}^2. \quad (3)$$

The solid line in Fig. 7a and Fig. 8b shows the fit of ν_S to eqn 3, giving $M_S \sin\theta' = 0.325$ T and D′ = 1.68 eVÅ^2 for both NCMO and PCMO for 180^o geometry. In the case of PCMO, different scattering geometry yields different $M_S \sin\theta'$, as the angle θ' is different for different scattering geometries. Hence we see different intercepts for different geometries. This gives a rough estimate of D ~ 0.84 eVÅ^2, which is higher than the value measured by inelastic neutron scattering in ferromagnetic phase of these manganites [15]. We should keep in mind that the S-mode is very weak and the range of $q_{\|}$ is limited, which makes the accurate determination of D and M_S difficult. A large value of $4\pi M_S$ also implies that the changes in frequency of the bulk and surface magnons due to the applied field up to 0.3 T will be very small, in agreement with our experiments.

We now discuss the temperature variation of the scattered light intensity from spin waves via fluctuations in the dielectric constant ε arising due to spin-orbit coupling to the spin fluctuations. The scattered intensity is [10],

$$I(\omega)\, \alpha\, (\gamma M_S/\omega)\, k_B T\, |GM_S \pm K|^2 \quad (4)$$

where G and K are magneto-optic constants coupling $\Delta\varepsilon$ to transverse component of the magnetization M_t and M_S: $\Delta\varepsilon = KM_t + GM_SM_t$. The ± signs refer to Stokes and antiStokes intensities. It can be seen that $I(\omega)$ will also follow the temperature-dependence of saturation magnetization, as seen in Fig. 6a as well as to some extent in Fig. 10a.

The linewidth Γ of the Brillouin line associated with spin waves arises from lifetime effects ($= 2/T_2$ for the transverse coupling, where $1/T_2$ is the spin–spin relaxation rate [16]) as well as from inhomogeneous broadening. This broadening is somewhat similar to that seen in electron spin-resonance [17]. The enhancement of G seen at T_{CO} can be due to critical magnetic fluctuations. The temperature-dependence of the linewidth of the spectral function for the spin autocorrelation function due to critical fluctuations is given by $\Gamma(q) = \Gamma_o(q)\, f(1/q\xi)$ where $\Gamma_o(q)$ is the linewidth at T_C and $f(x)$ is a homogeneous complicated function of x [18]. Here, ξ is the correlation length which diverges as $\xi \sim (T - T_C)^{-\nu}$, with $\nu \sim 0.6$. The function $f(x)$ is nonmonotonic; it decreases as x decreases till $1/q\xi \sim 1$, but for lower values of $1/q\xi$ (i.e. $T \rightarrow T_C$), it increases. The enhancement of the Brillouin linewidth as T decreases from 300 to 250 K (Figs 6b and 10b) corresponds to the increase in the function $f(1/q\xi)$ below $(q\xi)^{-1} < 1$.

A few words on why we do not see magnons due to the AFM state would be appropriate. The zero wave vector bulk magnon in antiferromagnet has frequency $\omega_B = \gamma(2\, B_E B_A + B_A^2)^{1/2}$, where B_E is the exchange field and B_A the anisotropy field [14]. Usually, $B_E >> B_A$ and therefore $\omega_B \sim \gamma\, (2B_E B_A)^{1/2}$. These frequencies are much higher than those in ferromagnet; for example $\omega_B \sim 8.7$ cm^{-1} in MnF_2 ($T_N \sim 100$ K) and $\omega_B \sim 52$ cm^{-1} in FeF_2. The scattering cross-section is proportional to $(B_A)^{1/2}$ and therefore, antiferromagnet tends to be much poorer light scatterer [14].

Our results clearly demonstrate that magnetic excitations associated with ferromagnets are present at all temperatures, even below T_N. This is somewhat surprising and can be understood on the basis of the following considerations. The large peak in χ at T_{CO} is attributed to FM correlations due to Zener double exchange mechanism [15], [19]. This is because below T_{CO}, the e_g electrons become self-trapped due to JT polarons. The resulting ordering of e_g orbitals allows strong super exchange interactions which gives rise to antiferromagnetism. However, above T_{CO}, the carriers are relatively free to move and the super exchange mechanism will be weak and locally undetermined. This allows Zener double exchange to operate. Another reason to see ferromagnetic magnons above T_{CO} could be the light scattering mechanism [16]. It is known that the transverse scattering cross-sections are usually much higher than the longitudinal ones below T_C corresponding to para to ferro transition as a result of nonzero spontaneous magnetization. Above T_C, both the cross-sections are equal. The interesting aspect of light scattering from magnetic excitations is that the transverse scattering cross-section above T_C (i.e. in para state) is nonzero. For example, in FM $CrBr_3$, intensity ratio $I(T)/I(T_C)$ is as high as ~ 0.6 for $T/T_C \sim 1.25$ [16]. This explains why we can observe spin wave excitations in the Brillouin spectra in PM phase above T_{CO}.

With regard to the presence of ferromagnetic magnons below T_{CO}, the recent report of a spin wave branch in neutron scattering experiments below T_N in $La_{1-x}Ca_xMnO_3$ ($x = 0.05$ and 0.08) is relevant [20], [21]. This low-energy branch, fitted to $\omega = \omega_o + Dq^2$, is attributed to magnetic excitations of a droplet with ferromagnetic correlation length of ~ 10 Å. Surprisingly, these spin excitations are well defined and have propagating character even at small q, i.e. over distances

larger than the droplet size. The presence of ferromagnetic excitations along with those of the AFM state have been related to the separation of the sample into two magnetic regions, induced by an electronic phase segregation. Our present results also support such a scenario in charge-ordered NCMO. The increase in the susceptibility below 100 K (see Fig. 5b) as well as seen in Fig. 5a can be understood either as a mixture of ferromagnetic domains in AFM background or as a canted AFM state [15].

5. Conclusions

In summary, bulk and surface magnetic excitations have been seen in the Brillouin scattering of NCMO and PCMO. These excitations are associated with ferromagnetic correlation over the temperature range of 300 to 27 K. The presence of ferromagnetic droplets below T_{CO} suggests electronic phase segregation, similar to the one proposed in other manganites. It would be of interest to carry out inelastic neutron scattering experiments on charge-ordered systems to look for ferromagnetic propagating modes below T_{CO}.

Acknowledgements

I would like to thank Dr P. Murugavel for the measurements and Profs A. K. Sood and C. N. R. Rao for their deep involvement and support in this work.

References

1. C. N. R. Rao and B. Raveau, In *Colossal magnetoresistance, charge-ordering and related properties of manganese oxides* (Rao, C. N. R. and Raveau, B., eds), World Scientific (1998).

2. P. M. Woodward, T. Vogt, D. E. Cox, A. Arulraj, C. N. R. Rao, P. Karen and A. K. Cheetham, Influence of cation size on the structural features of $Ln_{0.5}A_{0.5}MnO_3$ perovskites at room temperature, *Chem. Mater*., **10**, 3652–3665 (1998).

3. C. Zener, Interaction between the d-shells in the transition metals. II. Ferromagnetic compounds of manganese with perovskite structure, *Phys. Rev*., **82**, 403–405 (1951).

4. P. W. Anderson and H. Hasegawa, Considerations on double exchange, *Phys. Rev*., **100**, 675–681 (1955).

5. A. J. Millis, P. B. Littlewood and B. I. Shraiman, Double exchange alone does not explain the resistivity of $La_{1-x}Sr_xMnO_3$, *Phys. Rev. Lett*., **74**, 5144–5147 (1995).

6. C. M. Verma, Electronic and magnetic states in the giant magnetoresistive compounds, *Phys. Rev. B*, **54**, 7328–7333 (1996).

7. S. Mori, C. H. Chen and S-W. Cheong, Paired and unpaired charge stripes in the ferromagnetic phase of $La_{0.5}Ca_{0.5}MnO_3$, *Phys. Rev. Lett*., **81**, 3972–3975 (1998).

8. S. Mori, T. Katsufuji, N. Yamamoto, C. H. Chen and S.-W. Cheong, Microstructure related to charge and orbital ordering in $Pr_{0.5}Ca_{0.5}MnO_3$, *Phys. Rev. B*, **59**, 13573–13576 (1999).

9. T. Vogt, A. K. Cheetham, R. Mahendiran, A. K. Raychaudhuri, R. Mahesh and C. N. R. Rao, Structural changes and related effects due to charge ordering in $Nd_{0.5}Ca_{0.5}MnO_3$, *Phys. Rev. B*, **54**, 15303–15306 (1996).

10. J. R. Sandercock, In *Light scattering in solids* (M. Cardona and G. Güntherodt, eds), Vol. III, Springer Verlag, pp.173–206 (1982).

11. R. Mahendiran, M. Hervieu, C. Martin, A. Maignan, V. Caignaert and B. Raveau, Hysteretic magnetic susceptibility of $Pr_{0.5}Ca_{0.5}MnO_3$: Correlation with modulated charge-orbital ordering (Preprint).

12. R. W. Damon and J. R. Eshbach, Magnetostatic modes of a ferromagnet slab, *J. Phys. Chem. Sol*., **19**, 308–314 (1961).

13. J. R. Sandercock and W. Wetting, Light scattering from surface and bulk thermal magnons in iron and nickel, *J. Appl. Phys*., **50**, 7784–7787 (1979).

14. M. G. Cottam and D. J. Lockwood, In *Light scattering in magnetic solids*, Wiley (1986).

15. D. E. Cox, P. G. Radaelli, M. Marezio and S.-W. Cheong, Structural changes, clustering, and photoinduced phase segregation in $Pr_{0.7}Ca_{0.3}MnO_3$, *Phys. Rev. B*, **57**, 3305–3314 (1998).

16. W. Hayes and R. Loudon, In *Scattering of light by crystals*, Wiley, pp. 239–291 (1978).

17. R. Gupta, J. P. Joshi, S. V. Bhat, A. K. Sood and C. N. R. Rao, An electron paramagnetic resonance study of $Pr_{0.6}Ca_{0.4}MnO_3$, *J. Phys.: Condensed Matter*, **12**, 6919–6926 (2000).

18. P. Resibois and C. Piette, Temperature dependence of the linewidth in critical spin fluctuation, *Phys. Rev. Lett.*, **24**, 514–516 (1970).

19. E. Pollert, S. Krupicka and E. Kuzmicova, Structural study of $Pr_{[1-x]}Ca_{[x]}MnO_{[3]}$ and $Y_{[1-x]}Ca_{[x]}MnO_{[3]}$ perovskites, *J. Phys. Chem. Sol.*, **43**, 1137–1143 (1982).

20. M. Hennion, F. Moussa, G. Biotteau, J. Rodriguez-Carvajal, L. Pinsard and A. Revcolevschi, Liquidlike spatial distribution of magnetic droplets revealed by neutron scattering in $La_{1-x}Ca_xMnO_3$, *Phys. Rev. Lett*., **81**, 1957–1960 (1998).

21. F. Moussa, M. Hennion, G. Biotteau, J. Rodriguez-Carvajal, L. Pinsard and A. Revcolevschi, Magnetic coupling induced by hole doping in perovskites $La_{1-x}Ca_xMnO_3$: A neutron scattering study, *Phys. Rev. B*, **60**, 12299–12308 (1999).